Ultramicroscopy 209 (2020) 112884

Contents lists available at ScienceDirect

Ultramicroscopy

journal homepage: www.elsevier.com/locate/ultramic

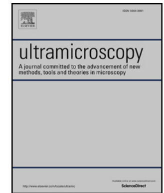

Imaging defect complexes in scanning transmission electron microscopy: Impact of depth, structural relaxation, and temperature investigated by simulations

Thomas Aarholt*, Ymir K. Frodason, Øystein Prytz

Department of Physics, Centre for Materials Science and Nanotechnology, University of Oslo, P. O. Box 1048, Blindern, N-0316 Oslo, Norway

1. Introduction

Doping of zinc oxide with donor atoms such as aluminium and gallium is common practice in realizing transparent conductive oxides (TCO) [1–4]. For high levels of doping, the formation of compensating donor-V_{Zn} complexes (vacancy on nominally Zn-site accompanying another defect) has been found to limit the *n*-type doping efficiency and thus the performance of ZnO as a TCO [5]. Understanding the exact optoelectronic effect of the defect complexes is important to further improve such devices. Electron Energy Loss Spectroscopy (EELS) in the low loss region can potentially be used to investigate the optical activity of such defects. However, the first step to measuring their signature in EELS is to accurately recognize them in the Scanning Transmission Electron Microscopy (STEM) image.

Three-dimensional imaging of single vacancies in extremely thin samples has been shown possible by High-Angle Annular Dark-Field (HAADF) STEM simulations [6]. Recent progress in CPU- and GPU-accelerated STEM algorithms [7–9] and user-friendly simulation software [10–12] has made it significantly more feasible to perform such simulations. The limits of detecting single dopant atoms have been discussed in the literature. Mittal et al. [13] discussed the visibility in Annular Dark-Field STEM (ADF-STEM) of a number of dopants over a series of sample thicknesses, pointing out how a Sn substitutional at the entrance surface and 5 nm below the entrance surface in 20 nm and 70 nm thick Si, respectively, can be more visible in the latter case. Primary-beam electron hopping between columns due to channelling and scattering has been shown to be a problem in determining the absolute composition of particles imaged by HAADF-STEM [9]. Therefore, it is essential to combine simulation and experiment to determine exact compositions. With regards to imaging single defects or defect complexes within a perfect crystal, the problem is slightly simplified. Since the neighbouring columns are of a known composition, the only significant variable is the depth position of the defect within the sample. Probe focus is set to Scherzer defocus, which on the sample is the focus that gives the sharpest image when imaging the bulk crystal.

Conventional simulation studies tend to use only a single detector to image defects. Instead of imaging a single defect with a single ADF detector, here we take advantage of a laterally-displaced common defect *pair,* $In_{Zn}V_{Zn}$ (indium substituted on zinc site next to a vacancy substituted on zinc site), of comparatively high and zero mass, as well as a multiple detector setup to find the most probable conditions for successfully measuring a defect's 3D-position.

Several authors [13–16] have shown how the STEM probe is prone to scatter back and forth between neighbouring atomic columns in an oscillating fashion. Hwang et al. [14] showed by STEM simulation that Cs-corrected probes are particularly prone to such scatter. In their $SrTiO_3$ example, the first maximum of probe intensity occurs at 0.8 nm, after which a significant fraction of the intensity scatters to neighbouring columns. After this maximum, direct and intuitive correlation of intensities with the sample atomic species becomes much more complex and increases uncertainty in estimating the species responsible for the scatter. This is not a problem when the sample is composed of a single element, as the scatter between columns is equal. Martinez et al. [17] show that for a Pt crystal the cross-section at medium and high scattering angle increases monotonically with sample thickness. However, for a binary alloy, this may not necessarily be the case, and for point-defects the effect of the scattering is unclear. Hence, a simulation-based approach can be appropriate when attempting to detect vacancy or substitution cases with very few atoms. In order to measure the intensity of a given column, the Absolute Integration feature of the Atomap [30] open-source Python software was used. The integrator, which has previously [31,32] been used for numerical studies on STEM images is a method based on Voronoi cell integration. Here, cells are allowed to “grow” from the position of the centre of each atomic column until each cell intersects another. The plotted intensity is then the sum of the counts beneath each cell. The technique requires relatively little computation power when compared to more common two-dimensional gaussian curve-fitting techniques and provides an image that is much easier to interpret than conventional high-resolution images.

* Corresponding author.
E-mail address: thomas.aarholt@smn.uio.no (T. Aarholt).

https://doi.org/10.1016/j.ultramic.2019.112884
Received 23 April 2019; Received in revised form 25 October 2019; Accepted 1 November 2019
Available online 04 November 2019
0304-3991/ © 2019 The Authors. Published by Elsevier B.V. This is an open access article under the CC BY-NC-ND license
(http://creativecommons.org/licenses/BY-NC-ND/4.0/).

2. Methodology

2.1. Simulation details

The Prismatic [8,10] STEM simulation software was used to perform the simulations. Prismatic can utilize both central (CPU) and graphical processing units (GPU), and always provides the full range of possible detector angles (0–95 mrad in this case) as output, with a given step, up to the maximum collection angle given by the potential spacing. The computers for the present simulations were three servers with 28-core Intel Xeon CPU, 128 GB of ram and four Nvidia GeForce RTX 2080TI graphics cards. With Prismatic we were able to quickly simulate images with and without a defect with a small (1 mrad) step in acceptance angle, in order to understand over which acceptance angle regime we should be measuring the defect.

To ensure accurate simulations, the potential pixel size p was set to 5 pm. This was smaller than the 8 pm spatial resolution (probe spacing) of the simulated electron beam, ensuring that the atoms did not appear pixelated. Since prismatic additionally uses an anti-aliasing aperture 0.5 times the maximum scattering angle, and the accelerating voltage was set to 300 kV, the effective maximum scattering angle was 98 mrad, according to Eq. (1).

$$\text{max scattering angle} = \frac{\lambda q}{2} \tag{1}$$

where $q = = 1/(2p)$ is the reciprocal-space pixel size of the real space potential grid spacing p and λ is the relativistic wavelength of the incoming electron. A final restriction is the angular resolution of the beam on the sample. Egerton [18] writes that the ratio of the incident beam semi-angle α should be at least ten times the angular resolution. This condition is described by Eq. (2),

$$\frac{\alpha}{\text{angular resolution}} = \frac{\alpha x}{\lambda} \geq 10 \tag{2}$$

where x is the shortest lateral sample length, 72 Å for our models. With the large cell size, the PRISM interpolation factor was set to 4, which gave fast simulation speeds with accurate results. For our simulations with $\alpha = 20$ mrad (and a PRISM alpha limit of 22 mrad), the ratio of α to angular resolution was 50.8. Simulations were performed with spherical aberration of 0.001 mm and the beam focused on the top surface of the samples and a slice thickness of 0.81 Å. It should be noted that in Prismatic, the beam hits the atoms with highest value of z first, and atoms at $z = 0$ last. This is the opposite convention of most other simulation software. Chromatic aberration due to the 0.9 eV energy spread of the incoming electron was included through a defocus series of five steps, equally spaced by the standard deviation of 48 Å, as seen in Fig. 1a.

2.2. Creating the defect models

As a starting point for the modelling, hexagonal unit cells of ZnO were transformed into orthogonal cells. The orthogonal angles of these cells made it easier to construct models. Supercells of 3 × 3 × 2 unit cells of orthogonal ZnO were then constructed, with dimensions $a = 9.73$ Å, $b = 11.24$ Å, $c = 10.38$ Å, and rotated to give an orientation with the beam-direction along the 100 zone axis. Defect cells were built based on these supercells. A *static* model of the In_{Zn}-V_{Zn} defect cluster was created by removal of a single Zn atom and substitution of In on a neighbouring Zn site on the 110 plane. This static model will give a first indication of the visibility of the defect cluster. However, it does not take into account the structural relaxation that inevitably takes place in the vicinity of all defects and defect clusters. Therefore, the atom positions in the static model were relaxed by density functional theory (DFT) to produce the *relaxed* model. Larger models for STEM simulation were constructed using the Atomic Simulation Environment [19] Python software.

DFT calculations were performed using the Heyd-Scuseria-Ernzerhof (HSE) [20,21] hybrid functional and the projector augmented wave method [22–24], as implemented in the VASP code [23–25]. The screening parameter was fixed to the standard value to $\omega = 0.2$ Å^{-1}, and the fraction of screened Hartree-Fock exchange adjusted to $\alpha = 0.375$ [26]. Defect calculations were performed with the 3 × 3 × 2 supercell by keeping the lattice parameters fixed and relaxing all atomic positions until the residual forces were reduced to less than 5 meV/Å. Using DFT to study relaxation of point defects is by far the most common of the techniques available [27]. The cut-off energy for the plane-wave basis set was set to 500 eV, and a special off-Γ k-point at $k = (¼,¼,¼)$ was used for integrations over the Brillouin zone. The maximum radial displacements from the static model in three-dimensions were 0.114 Å and 0.311 Å for Zn and O, respectively. Of the three-dimensional displacement, most was in the lateral direction, perpendicular to the beam direction. The maximum lateral displacements were 0.104 Å and 0.311 Å. While the DFT calculations are performed at 0 K, experimental studies on ZnO show that when increasing the temperature from 20 K to 300 K, the lattice spacings only increase by 0.02 Å [28]. We therefore believe that the effect of temperature will be negligible on the relaxed positions.

To model the defect as a function of depth, 6 supercells of pristine ZnO were stacked along the beam direction, and the defect supercell was inserted into the bulk at increasing depths, with steps of 1/3 of the supercell thickness. The total sample thickness was approximately 3.2 nm. Once the defect structure was built, pristine ZnO was stacked laterally to give sample width and height of 50 nm. Fig. 2 shows the structure of the relaxed supercell, with labels indicating the defect-containing columns.

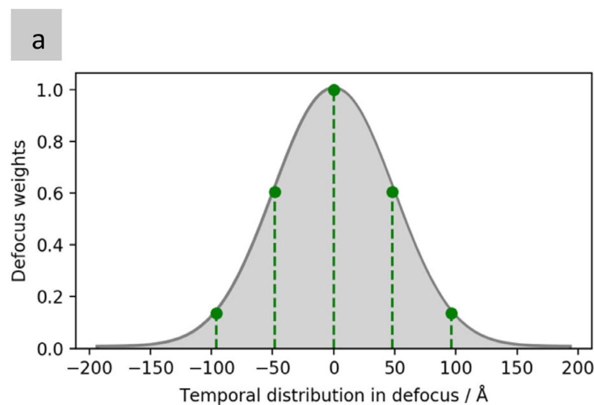

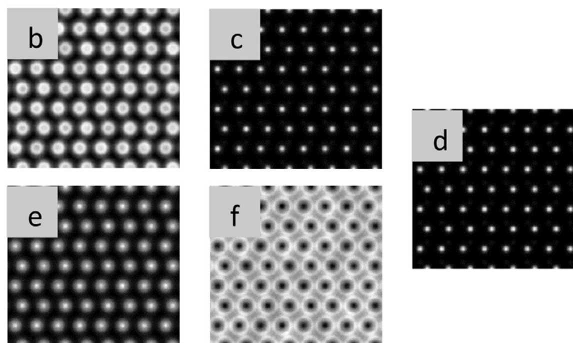

Fig. 1. (a) Defocus series distribution according to an energy spread of 0.9 eV. Chromatic aberration is approximated by weighted averaging of the resultant STEM images from five defocus values chosen 1 standard deviation (48 Å) apart. The resulting images on bulk ZnO at room-temperature, are shown in b-e, for defocus of values from −96 through +96 Å in steps of 48 Å.

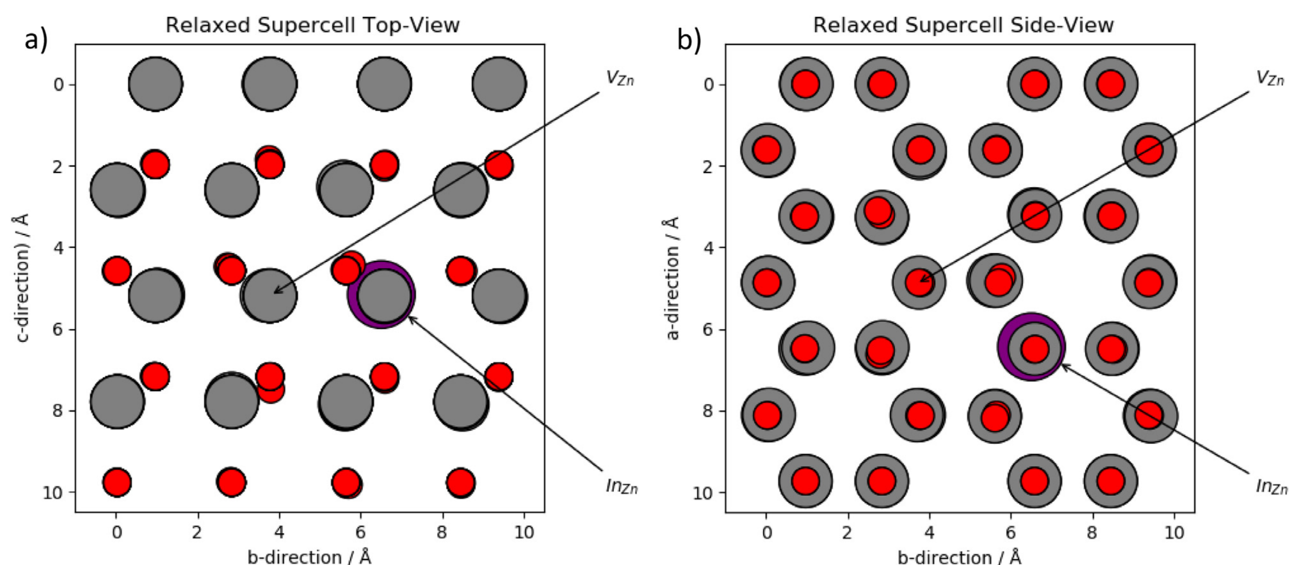

Fig. 2. Top-view (left, along 100) and side-view (right, along 001) representation of the defect supercell. Labels indicate defect-containing columns.

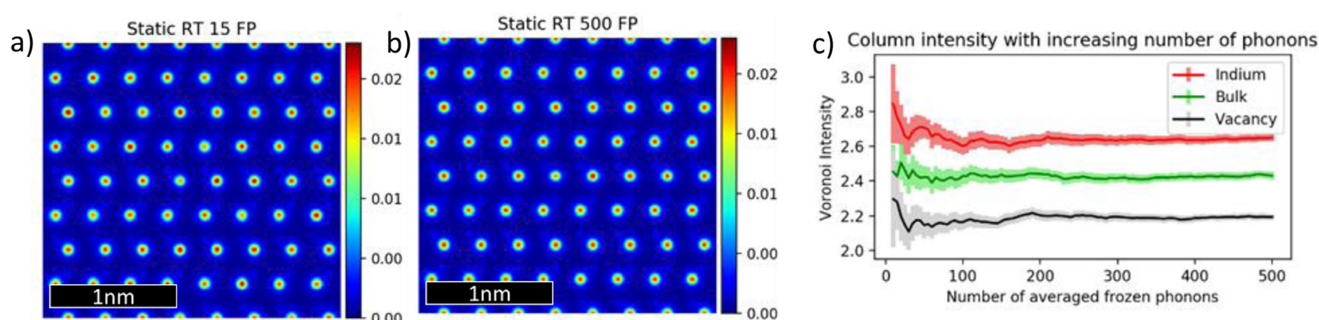

Fig. 3. HAADF simulation of the static defect model at room temperature at depth 1 with (a) 15 and (b) 500 frozen phonons (FP). (c) Mean of Voronoi intensity by with increasing number of frozen phonons on the static defect at depth 1. The “Bulk” value here is taken as one of the edge columns on the image furthest from the defect. Error bars are one Standard Deviation of the Mean (SDOM).

While for larger models, 20–40 Frozen Phonon (FP) configurations are often enough to produce a realistic simulation, the thin specimen model of this work demanded a much higher number of FP configurations. To estimate the necessary number of FPs, convergence testing was performed on bulk ZnO. These simulations were performed on a region of interest (ROI) containing 30 columns of ZnO of the same thickness as the defect models. Each frozen phonon configuration was generated by random lateral displacement of the atom according to its Debye Waller factor (shown in Table 2) by the Prismatic software.

Fig. 3 shows the intensity for 42 atomic columns, centred around the static defect model. The right-hand graph shows the Voronoi integrated intensity (introduced in the next section) as a function of increasing number of frozen phonons. For these thin specimens 100 phonon configurations, laterally displaced, were shown to be sufficient to minimize error. Since each image is composed of the weighted average of a defocus series with five values, each image consists of 500 frozen phonon iterations. The error bars represent the Standard Deviation of the Mean (SDOM) and were computed in the following way: First, the positions of the atoms were determined using the Atomap software on a sum image of the bulk ZnO model. The sum image was calculated by first averaging the five defocus sets of 100 frozen phonon images to produce five images, one for each defocus value. The five images were averaged with weights (according to Fig. 1) to produce a single “sum image” that was fed to Atomap to determine the positions. The Voronoi grid was then calculated and applied to the HAADF and MAADF datasets (of 100 defocus-averaged images) to produce, for each column in the image, a list of intensities 100 values long. The SDOM was then measured by calculating the standard deviation of the list divided by the square root of the number of entries.

2.3. Analysis details

Each frozen phonon image resulted in a spectrum image with a file size of 28 MB. The 30 models simulated with 500 phonons totalled over 400 GB of data. To load such large datasets, the lazy loading capability of the HyperSpy [29] open-source Python software was employed, which made it possible to manipulate large data without loading it all into memory simultaneously. The Atomap software, with which we employed the Absolute Integrator technique, is built on top of the HyperSpy framework, which made it very simple to process the data. The smallest lateral distance between the Zn columns of the simulated model is 2.7 Å. This is larger than the 2 Å minimum distance recommended by De Backer et al. [33] for analysis like Voronoi cell integration that does not take peak overlap (such as could be fitted by two gaussians) into account. In its Atomap implementation, Voronoi integration can be limited to within circles of given radii, in order to prevent edge-effects from interfering with the region of interest. In the present work, simulation was performed on an area large enough to facilitate full Voronoi integration. The Voronoi cells from columns at the edge of the images were removed as their areas differed due to interaction with the image border. Automatic removal of such edge effects, along with significant performance increases have been merged into the Atomap software by the authors.

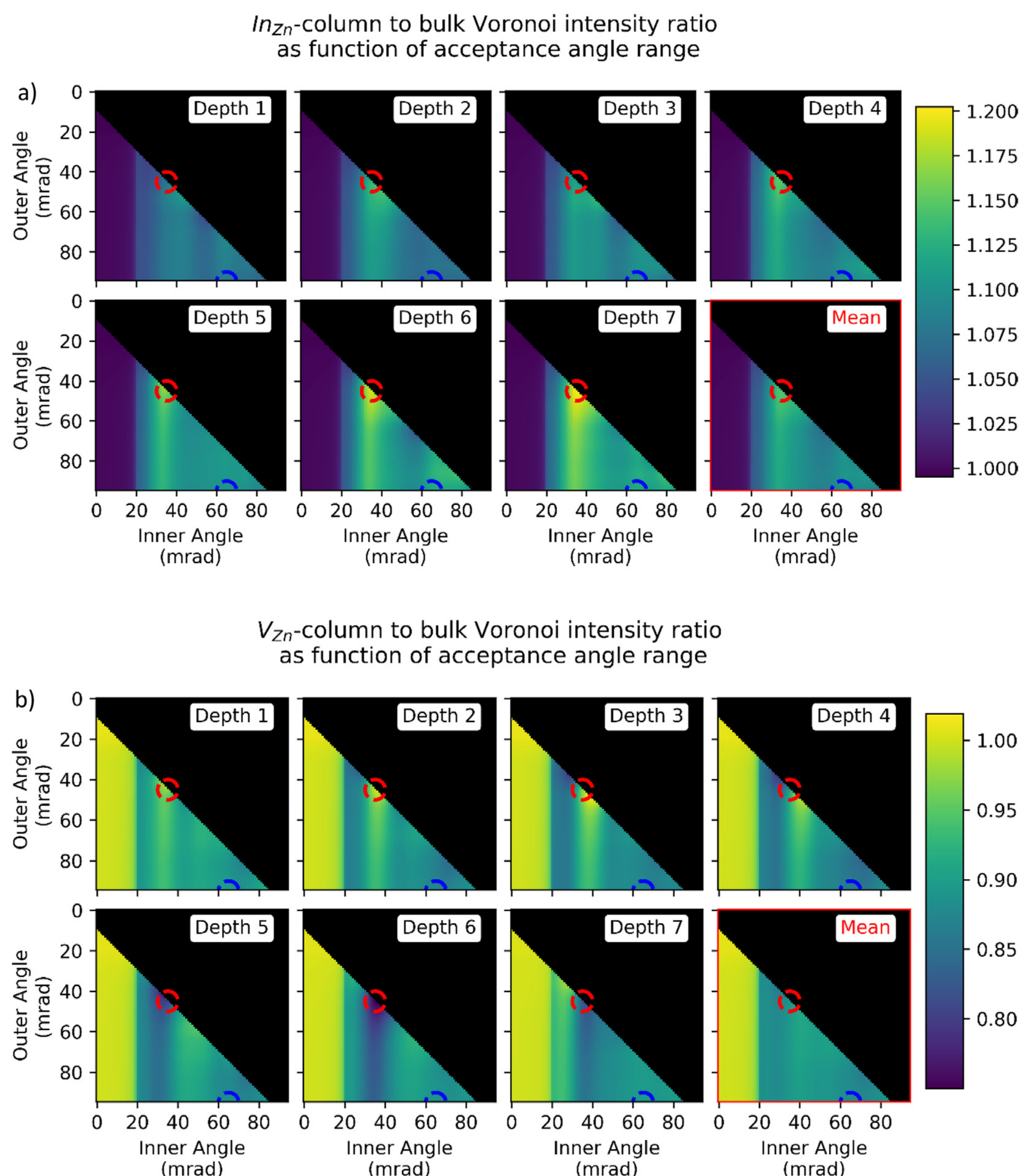

Fig. 4. Contrast maps of the Voronoi intensity of relaxed a) In_{Zn} and b) V_{Zn} columns divided by bulk Zn column as a function of inner and outer acceptance angles. The red and blue circles indicate the respective positions of the MAADF (35–45 mrad) and HAADF (65–95 mrad) ranges chosen.

2.4. Choosing optimal acceptance angles

STEM instruments have annular detectors that are fixed at a certain distance, and hence angle, from the specimen. Instruments that have post-specimen lenses can control the camera length from the specimen, which in turn affects the inner and outer acceptance angle for a given annular detector. On high-end STEM instruments, it is not unusual to have three or four annular detectors covering several ranges of acceptance angles, which can all simultaneously record images. These, combined with the ability to change camera length give rise to a high number of possible acceptance angles. If the microscope configuration allows it, this can be further enhanced by shadowing one detector by another, thereby reducing the outer acceptance angle on the detector furthest from the specimen.

To determine the acceptance angles giving the highest contrast between pristine and defected ZnO regardless of defect depth position, bulk and relaxed models were simulated across acceptance angles from 0 to 95 mrad in steps of 1 mrad, with a minimum detector width of 10 mrad to give ranges that could be realistically obtained. We then calculated STEM images for all possible acceptance ranges, 0–10, 0–11 …, 84–95, 85–95 mrad. The Voronoi integration method was applied to all images, using the known lateral position of Zn-containing columns from the bulk model. Finally, the Voronoi intensity from the In_{Zn} and V_{Zn} columns of the relaxed model was divided by the average equivalent intensity of Zn columns of the bulk model. These contrast maps are plotted in Fig. 4, showing the ratio as a function of inner and outer angle. Each image shows the contrasts at a separate depth position of the defect with the final image showing the mean of the seven depth positions. The colour bar shows the ratio of defect column to bulk column, and all depth positions are plotted with the same colour range.

The contrast values reveal that at low acceptance angles (up to the convergence angle) there is essentially zero contrast (ratio of 1) between the bulk and relaxed models. The strongest contrast is found at medium inner angles starting at around 25 mrad and is shown to become more intense as the defect is positioned lower in the sample. At high angles the contrast is nearly uniform with depth position, with a

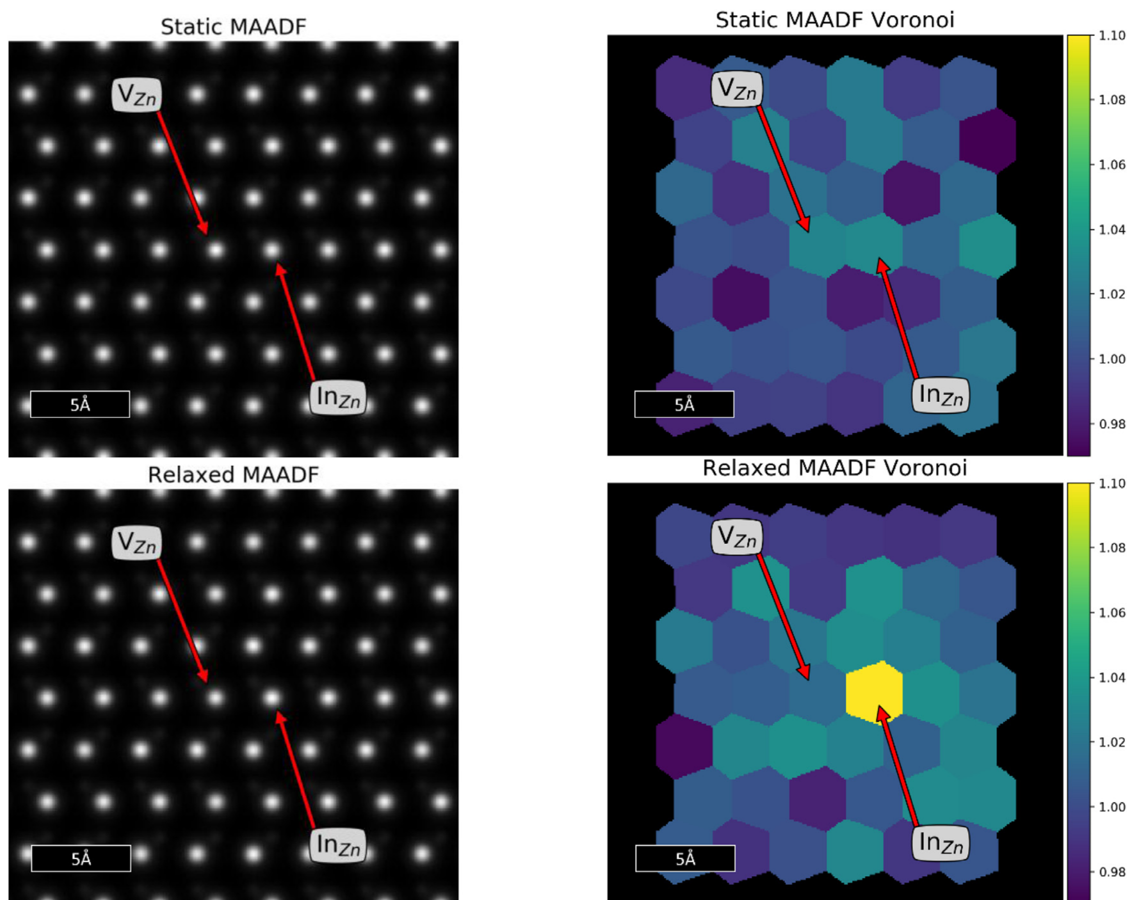

Fig. 5. Conversion of simulated MAADF image of the model of the In_{Zn}-V_{Zn} defect complex in ZnO (left) to the intensity image by Voronoi-integration (right), taken from a simulation with the defect at position 2. Top: Static model. Bottom: Relaxed model. The In_{Zn} and V_{Zn}-containing columns are highlighted. The relaxed model shows much higher intensity on the In_{Zn} column than that of the static model. Note that the contrast limits on this image are narrower than those on Fig. 7 in order to highlight the change.

slight peaking near 80–95 mrad for the lowest depths.

As the contrast showed significant change with depth position at the 35–45 mrad range, we decided to use this position to track the depth-position of the defect. Meanwhile, a range from 65 mrad and up was chosen in order to track the defect laterally on the sample as the contrast maps show that the intensity of the columns is vacancy column < bulk column < In column regardless of defect position. Hence, the indium column and vacancy column should be consistently brighter and darker than the bulk, respectively.

Acceptance angles in the range 65–95 mrad are typical of the HAADF detector on the microscope, following the rule of thumb of an inner angle larger or equal to 3α [34]. With the chosen convergence angle of 20 mrad, acceptance angles in the range 35–45 mrad are detectable on an ADF detector placed in this range, possibly shadowed by another detector. We henceforth refer to these images as Medium-Angle Annular Dark-Field (MAADF) images. MAADF images typically contain a mix of diffraction contrast and atomic number contrast, which are sensible contrast mechanisms for the material system we are investigating. With realistic acceptance angles to construct the STEM images, the differences between STEM simulation on the static and relaxed defect structures were calculated.

3. Results

3.1. Comparing DFT-relaxed defect cell with static defect cell

The effect and importance of the structural relaxation is difficult to see by eye on the standard STEM image, but the differences become clear by numerical analysis. Fig. 5 shows the differences in intensity of the static (top) and relaxed (bottom) cells, showing both the raw MAADF STEM simulation but also the integrated Voronoi image. The intensities summed in the Voronoi images have been normalised by the equivalent intensity for pure ZnO. While the column containing the single In atom is clearly seen, there is little or no change in the intensity on the neighbouring columns around the defect.

Voronoi cell integration of high-resolution STEM images is here shown to be an efficient method to simplify identification of changes to column intensity without resorting to curve fitting or maxima approaches. While the method yields less information (such as the width of the column) than conventional curve-fitting algorithms, it is much faster and can be performed on very large datasets in a matter of seconds. However, it is important to note that it requires sufficient spatial resolution (80 pm was determined to be enough for this work) not to introduce sampling artefacts, and datasets acquired experimentally must be done so with long enough exposure to minimize noise.

3.2. Effect of defect depth position on contrast

To further investigate the intensity variation caused by the defect, images were simulated as a function of the defect's position along the beam path (depth). To preserve the relaxation around the defect, the first depth position containing the indium defect was the fifth layer. Then, the defect supercell was stepped down throughout the bulk model until the indium defect reached the second layer from the bottom of the model. A schematic of this is shown in Fig. 6(c).

After Voronoi-integration, the intensities of the two defect-

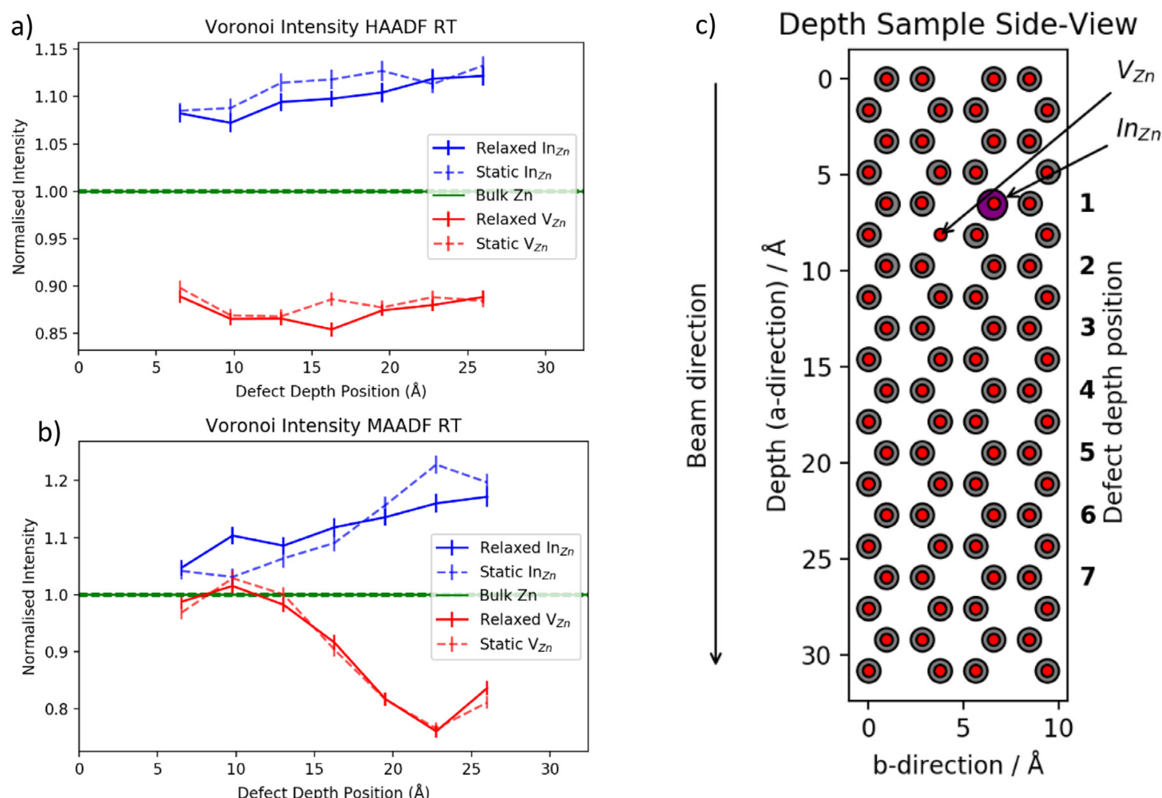

Fig. 6. (a) Integrated HAADF intensity over the atomic columns as a function of depth position of the defect complex for a static and DFT-relaxed model with 500 frozen phonon configurations at room-temperature. (b) Same as a) but for the MAADF signal. Error bars are one standard deviation of the mean. (c) Schematic of a cross-section of the sample showing the defect position. The right-hand axis shows the position of the In_{Zn} of the defect complex as the complex is stepped throughout the sample.

Table 1
Table of ratios of the room-temperature intensities of the two defect columns to the average bulk ZnO column taken from Fig. 6(a) and (b).

		Defect column ratio to average bulk column at RT					
		HAADF	MAADF				
Model	Defect	Mean	Min	Max	Mean	Min	Max
Relaxed	In	1.10	1.07	1.12	1.12	1.05	1.17
	V	0.87	0.85	0.89	0.90	0.76	1.02
Static	In	1.11	1.09	1.13	1.12	1.03	1.23
	V	0.88	0.87	0.90	0.90	0.77	1.03

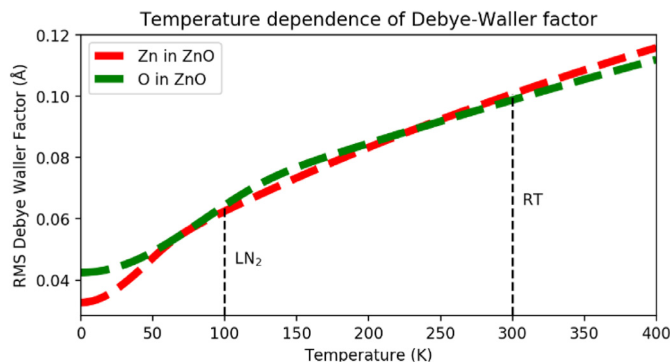

Fig. 8. Temperature-dependence of Zn and O in ZnO based on a model by [36].

containing columns were normalised by the bulk mean and plotted in Fig. 6, as a function of depth. The HAADF signal shows typical Z-contrast, displaying intensities of the expected trend of In_{Zn} > Bulk > V_{Zn} due to the atomic number of the atoms and number of atoms present in the column. The mean, minimum and maximum values for each column type are listed in Table 1, shown relative to the average bulk ZnO

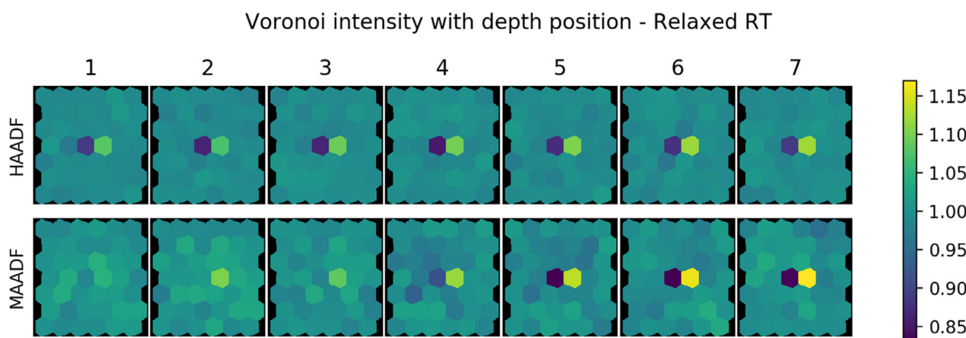

Fig. 7. Voronoi intensity on the relaxed model at room temperature with increasing depth. HAADF (top row) and MAADF (bottom row) images share the same colour bar. The contrast limits are slightly narrower than the minimum and maximum values in the image (0.76–1.17), in order to highlight intensity variations in first depth positions and be directly comparable to Fig. 10.

Table 2
Values of the root-mean-square Debye-Waller factor at 300 and 100 K from [36].

Temperature (K)	RMS Debye-Waller Factor (Å)	
	Zn	O
300	0.101	0.099
100	0.062	0.064

Table 3
Table of ratios of the liquid-nitrogen temperature intensities of the two defect columns to the average bulk ZnO column taken from Fig. 9a) and b).

		Defect column ratio to average bulk column at LN2					
		HAADF	MAADF				
Model	Defect	Mean	Min	Max	Mean	Min	Max
Relaxed	In	1.12	1.08	1.17	1.14	1.05	1.25
	V	0.90	0.88	0.94	0.93	0.64	1.19
Static	In	1.13	1.09	1.17	1.11	0.96	1.32
	V	0.90	0.87	0.93	0.91	0.62	1.14

column.

The indium-containing column (hereafter “In-column”) is on average 10% brighter than the average bulk column, with small variations of the intensities with defect depth position. The vacancy-containing column (“vacancy-column”) displays similar behaviour with an average of 13% lower intensity. This is beneficial for locating the defect laterally on the sample but is of no value in determining its depth-position. There is little difference between the static and relaxed models for the HAADF signal.

The MAADF signal shows strong variation in intensity with depth, particularly for the vacancy-column. When near the top of the sample, the defect complex (particularly the vacancy column) is virtually indistinguishable from the average bulk intensity in the MAADF image, whilst intense in the HAADF. However, as the defect moves down through the sample it increases significantly in MAADF intensity. When located at the penultimate position, the In-column is 16% and 23% brighter than the bulk column for the relaxed and static models, respectively. For the same position the vacancy-column is very symmetric in intensity, being 24% and 23% dimmer. This variation in intensity makes it possible to determine the approximate depth-position of the defect.

The change in defect intensity is even more clearly visualised by looking at the Voronoi image as a function of depth. Fig. 7 shows the Voronoi intensity for HAADF (top row) and MAADF (bottom row) normalised for the bulk mean. Here it is clear that the MAADF pattern created by the defect becomes stronger with increasing depth, with the In-column column becoming visible first. The columns surrounding the defect show no significant change in intensity at room-temperature.

3.3. Discussion

The HAADF intensity is mostly independent with the depth-position of the defect. This is in agreement with previous results [6]. However, for the relaxed In-column at both room and liquid-nitrogen temperatures, the HAADF intensity increases gradually with depth of the defect, reaching its maximum at the bottom of the sample. This is seen in Fig. 6. Zhang et al. [35] provide a likely explanation of the increase by electron channelling. They argue that as the incident probe channels along a column, atoms deeper in the foil see a more focused probe and consequently scatter to higher angles due to the closer proximity of the probe to the nucleus. This explains the brighter column intensity of the heavy In defect with depth. The vacancy-column is dimmest when the vacancy is in the middle of the sample, becoming slightly brighter at the edges. This is possibly due to the vacancy disrupting the effect of the channelling-focused probe, causing scatter to lower angles instead.

The MAADF intensity has been found to vary significantly with depth position, and alongside the lateral position gained from the HAADF intensity, allows for a three-dimensional measurement of the defect position. This work complements similar analysis done by Johnson et al. [6] on single point-defects, here showing the effect on defect complexes rather than individual point defects. The depth variation is likely due to a shift in scattering angle as the defect proceeds deeper into the sample. The bright regions in the MAADF range (near the red MAADF circle indicator) on Fig. 4 for both defects show a clear trend to the right with depth position, confirming this suspicion. It is possible that the same effect described by Zhang et al. [35] for the HAADF regime is present here.

The structural relaxation reduces the In-column HAADF intensity for nearly every depth position. This reduction can be attributed to the lateral shift of the indium atom with respect to the channelling-focused probe. Since the probe no longer targets the centre of the atom, this reduces the likelihood of the high-angle electron-nucleus scattering associated with the HAADF imaging.

3.4. Effect of temperature on sample

STEM instruments often have the addition of cooling holders to cool the sample down using liquid-nitrogen, typically to about 100 K. To investigate the effect of cooling on the STEM intensity, we repeated the defect depth-study with Debye-Waller factors for ZnO at 100 K instead of 300 K. A temperature-dependent model for the Debye-Waller factor of Zn and O in ZnO is given by [36], and is plotted in Fig. 8. The values of the Debye-Waller factor chosen for simulation are shown in Table 2. The value for the In_{Zn} defect was set equal to the Zn value, since no

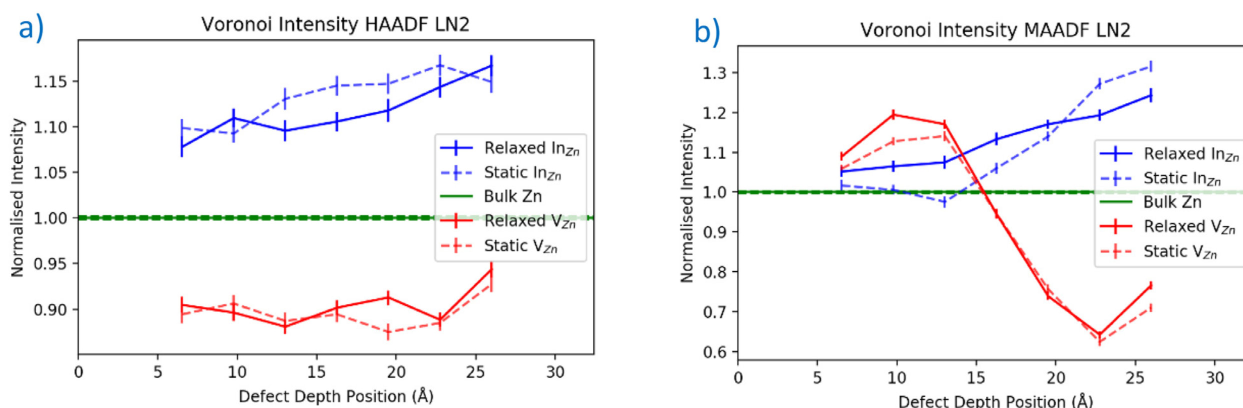

Fig. 9. (a) Integrated HAADF intensity over the atomic columns as a function of depth position of the defect complex for a static and DFT-relaxed model with 500 frozen phonon configurations at liquid-nitrogen temperature. (b) Same as (a) but for the MAADF signal. Error bars are one standard deviation of the mean.

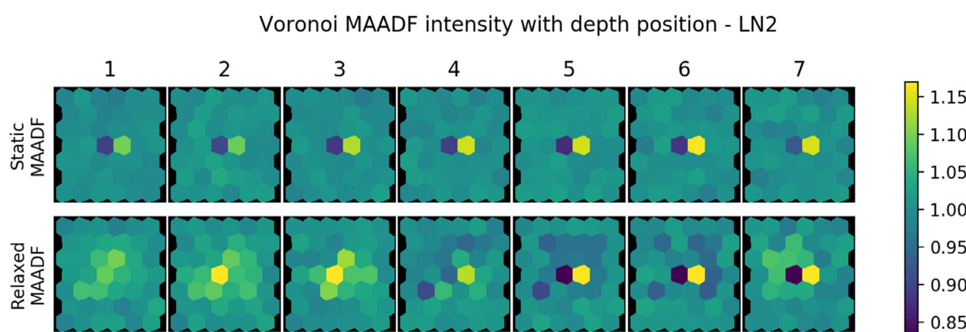

Fig. 10. Voronoi MAADF intensity on the Static (top row) and Relaxed (bottom row) model at liquid-nitrogen temperature with increasing depth. Both sets of images share the same colour bar. The effect on surrounding columns is only seen for the relaxed defect. The contrast limits are narrower than the minimum and maximum values in the image (0.62–1.24), in order to highlight intensity variations in first depth positions and be directly comparable to Fig. 7.

Debye-Waller value was available for the In defect and the Zn and O values were very close, despite their difference in atomic number.

The Voronoi-integrated intensities of the same columns as shown in Fig. 6 are shown in Fig. 9 but for liquid-nitrogen temperatures. A table summarising the mean, minimum and maximum for each defect column is shown in Table 3. The liquid-nitrogen HAADF results are similar to the room-temperature results, but with an overall increase in intensity of the defect columns relative to the bulk. This shifts the In-column up from the bulk average but reduces the intensity gap between the bulk and the vacancy-column. For both temperatures, the In-column shows an increasing intensity with depth position, but this behaviour is not seen for the vacancy-column. The MAADF intensity is greatly changed. For the first three depth positions, the vacancy-column is brighter than the In-column. At deeper positions, the defect increases strongly in intensity relative to the room-temperature simulation. At its highest, the relaxed In-column is 85% brighter than the relaxed vacancy-column.

The structural relaxation has approximately the same impact on the defect columns at liquid-nitrogen temperatures as at room-temperature but reduces the HAADF In-column intensity more at the lower temperature. The vacancy-column shows only a small relaxation impact on the MAADF image. The second and third depth position are brighter than expected by the static model, but for all other depths the vacancy appears nearly identical. Noticeably, there is a contrast reversal at depth-position 4, where the vacancy-column becomes darker than its counterpart.

There is a significant change in intensity on the columns *surrounding* the defect on the relaxed model at liquid-nitrogen temperature, as seen in Fig. 10. This effect is not seen on the static model, any HAADF image or on the simulations done at room-temperature, but only visible on the relaxed model MAADF image at liquid-nitrogen temperature. This effect is seen not only at lower depth positions, where contrast is high, but is noticeable as a slightly bright region on the first depth positions.

4. Discussion

The measurements at liquid-nitrogen temperature show a bigger difference between the relaxed and static models than for the measurements at room-temperature. The biggest change is found on the In column. We argue that the change in intensity is due to the reduced thermal vibration of atoms at the 100 K temperature, as seen by the much lower Debye-Waller factor of Zn and O at 100 K. Since the thermal movement of the atoms is smaller at 100 K than at 300 K, the small displacements caused by relaxation become more significant at the low temperature regime. The smaller change on the vacancy column is expected due to the lack of a temperature effect associated with the vacancy.

The change in MAADF intensity of the neighbouring columns at liquid-nitrogen temperatures due to defect relaxation is a novel important observation. The intensity change makes it easier to spot such defects, but also implies that other types of defects may cause significant intensity changes on several columns at liquid-nitrogen temperatures. Hence, depending on the type of defect one wishes to measure, it may be either an advantage or a disadvantage to image using a cooling holder. More types of defects would need to be investigated to determine whether this is a general phenomenon. An additional challenge with cooling holders is performing high-resolution imaging with the thermal drift due to temperature gradients across the sample and holder. This problem can be reduced by rigid registration of multiple frames, as demonstrated by Savitzky et al. [37] who achieved information transfer at 0.72 Å on a liquid-nitrogen cooled sample.

5. Conclusions

We have shown that it is possible to determine the three-dimensional position information of a defect complex in ZnO by STEM. A multi-detector configuration with specific acceptance angles is particularly helpful to maximise contrast and the chance of detecting the defect. By computing the intensity ratio of defect to bulk across possible acceptance angles the specific angles are determined. While the lateral position of the defects could be determined via conventional Z-contrast techniques on HAADF images (showing an apparent increase or decrease in thickness on the defect-containing columns), we have shown that STEM simulation is essential to determine the depth-position within the sample from experimental STEM images. The impact of a DFT-relaxed simulation model is shown to be particularly important for simulations with low Debye-Waller factors, with regards to the elements involved and for temperature-study considerations. With the high energy-resolution present in the newest generation monochromated STEM instruments, low noise in energy filter cameras, and true measurements of the position of a defect described in this paper, it should be possible to begin investigating the optical and electronic properties of such defects by EELS measurements.

Declaration of Competing Interest

The authors declare that they have no known competing financial interests or personal relationships that could have appeared to influence the work reported in this paper.

Acknowledgements

The authors are grateful to Rolf Erni, Ivan Lobato, Alan Pryor and Colin Ophus for valuable discussion and help with simulation software.

The authors would like to acknowledge support from the Research council of Norway through the Norwegian Center for Transmission Electron Microscopy, NORTEM (197405/F50), the Norwegian Micro- and Nano-Fabrication Facility, NorFab (197411/V30), and the FriPRO Toppforsk project FUNDAMeNT (no. 251131). DFT computations were performed on resources provided by UNINETT Sigma2 - the National Infrastructure for High Performance Computing and Data Storage in Norway. STEM simulation was performed on hardware generously provided by the University of Oslo AI Hub.

Supplementary materials

Supplementary material associated with this article can be found, in the online version, at 10.1016/j.ultramic.2019.112884.

References

[1] O. Ü, H. D, H. Morkoç, ZnO devices and applications: a review of current status and future prospects, Proc. IEEE 98 (7) (2010) 1255–1268.
[2] N.J. ichi, K. M, K. Okada, T. Ito, T. Miyata, T. Minami, Comparative study of resistivity characteristics between transparent conducting AZO and GZO thin films for use at high temperatures, Thin Solid Films 518 (11) (2010) 2937–2940, https://doi.org/10.1016/j.tsf.2009.10.134 Available from.
[3] T. Minami, Present status of transparent conducting oxide thin-film development for Indium-Tin-Oxide (ITO) substitutes, Thin Solid Films 516 (17) (2008) 5822–5828.
[4] T. Minami, H. Sato, H. Nanto, S. Takata, Group iii impurity doped zinc oxide thin films prepared by rf magnetron sputtering, Jpn. J. Appl. Phys. 24 (10) (1985) L781–L784.
[5] K.M. Johansen, L. Vines, T.S. Bjørheim, R. Schifano, B.G. Svensson, Aluminum migration and intrinsic defect interaction in single-crystal zinc oxide, Phys. Rev. Appl. 3 (2) (2015) 1–12.
[6] J.M. Johnson, S. Im, W. Windl, J. Hwang, Three-dimensional imaging of individual point defects using selective detection angles in annular dark field scanning transmission electron microscopy, Ultramicroscopy 172 (2017) 17–29, https://doi.org/10.1016/j.ultramic.2016.10.007 Available from.
[7] I. Lobato, S. van Aert, J. Verbeeck, Progress and new advances in simulating electron microscopy datasets using Multem, Ultramicroscopy 168 (2016) 17–27, https://doi.org/10.1016/j.ultramic.2016.06.003 Available from.
[8] A. Pryor, C. Ophus, J. Miao, A streaming multi-gpu implementation of image simulation algorithms for scanning transmission electron microscopy, Adv. Struct. Chem. Imaging (2017) Available from http://arxiv.org/abs/1706.08563.
[9] L.J. Allen, A.J. D'Alfonso, S.D. Findlay, Modelling the inelastic scattering of fast electrons, Ultramicroscopy 151 (2015) 11–22, https://doi.org/10.1016/j.ultramic.2014.10.011 Available from.
[10] C. Ophus, A fast image simulation algorithm for scanning transmission electron microscopy, Adv. Struct. Chem. Imaging 3 (1) (2017) 13. Available from http://ascimaging.springeropen.com/articles/10.1186/s40679-017-0046-1.
[11] I. Lobato, D. Van Dyck, MULTEM: a new multislice program to perform accurate and fast electron diffraction and imaging simulations using Graphics Processing Units with Cuda, Ultramicroscopy 156 (2015) 9–17, https://doi.org/10.1016/j.ultramic.2015.04.016 Available from.
[12] J.O. Oelerich, L. Duschek, J. Belz, A. Beyer, S.D. Baranovskii, K. Volz, STEMsalabim: a high-performance computing cluster friendly code for scanning transmission electron microscopy image simulations of thin specimens, Ultramicroscopy 177 (2017) 91–96, https://doi.org/10.1016/j.ultramic.2017.03.010 Available from.
[13] A. Mittal, K.A. Mkhoyan, Limits in detecting an individual dopant atom embedded in a crystal, Ultramicroscopy 111 (8) (2011) 1101–1110, https://doi.org/10.1016/j.ultramic.2011.03.002 Available from.
[14] J. Hwang, J.Y. Zhang, A.J. D'Alfonso, L.J. Allen, S. Stemmer, Three-dimensional imaging of individual dopant atoms in $SrTiO_3$, Phys. Rev. Lett. 111 (26) (2013) 1–5.
[15] R. Ishikawa, A.R. Lupini, S.D. Findlay, T. Taniguchi, S.J. Pennycook, Three-dimensional location of a single dopant with atomic precision by aberration-corrected scanning transmission electron microscopy, Nano Lett. 14 (4) (2014) 1903–1908.
[16] P.M. Voyles, D.A. Muller, J.L. Grazul, P.H. Citrin, H.J.L. Gossmann, Atomic-scale imaging of individual dopant atoms and clusters in highly n-type bulk Si, Nature 416 (6883) (2002) 826–829.
[17] G.T. Martinez, K.H.W. van den Bos, M. Alania, P.D. Nellist, S. Van Aert, Thickness dependence of scattering cross-sections in quantitative scanning transmission electron microscopy, Ultramicroscopy 187 (2018) 84–92, https://doi.org/10.1016/j.ultramic.2018.01.005 Available from.
[18] R. Egerton, Electron Energy-Loss Spectroscopy in the Electron Microscope, third ed., Springer, US, 2011.
[19] A.H. Larsen, et al., The atomic simulation environment — a Python library for working with atoms, J. Phys. Condens. Matter. 29 (2017) 273002.
[20] V. Krukau A, O.A. Vydrov, A.F. Izmaylov, G.E. Scuseria, Influence of the exchange screening parameter on the performance of screened hybrid functionals, J. Chem. Phys. 125 (22) (2006) 0–5.
[21] J.P. Perdew, K. Burke, M. Ernzerhof, Generalized gradient approximation made simple, Phys. Rev. Lett. 77 (18) (1996) 3865–3868.
[22] P.E. Blöchl, Projector augmented-wave method, Phys. Rev. B 50 (24) (1994) 17953–17979.
[23] G. Kresse, J. Hafner, Ab initio molecular dynamics for liquid metals, Phys. Rev. B 47 (1) (1993) 558–561.
[24] G. Kresse, D. Joubert, From ultrasoft pseudopotentials to the projector augmented-wave method, Phys. Rev. B 59 (3) (1999) 1758–1775.
[25] G. Kresse, J. Furthmuller, Efficient iterative schemes for ab initio total-energy calculations using a plane-wave basis set, Phys. Rev. B 54 (16) (1996) 11169–11186.
[26] F. Oba, A. Togo, I. Tanaka, J. Paier, G. Kresse, Defect energetics in ZnO: a hybrid Hartree-Fock density functional study, Phys. Rev. B – Condens. Matter Mater. Phys. 77 (24) (2008) 3–8.
[27] C. Freysoldt, B. Grabowski, T. Hickel, J. Neugebauer, G. Kresse, A. Janotti, et al., First-principles calculations for point defects in solids, Rev. Mod. Phys. 86 (Mar (1)) (2014) 253–305.
[28] J. Albertsson, S.C. Abrahams, A. Kvick, Atomic displacement, anharmonic thermal vibration, expansivity and pyroelectric coefficient thermal dependences in ZnO, Acta Crystallogr. Sect. B 45 (1) (1989) 34–40.
[29] F. de la Peña, V.T. Fauske, P. Burdet, T. Ostasevicius, M. Sarahan, M. Nord, et al. Hyperspy software package [Internet]. (2018). Available from: 10.5281/zenodo.54004.
[30] M. Nord, P.E. Vullum, I. MacLaren, T. Tybell, R. Holmestad, Atomap: a new software tool for the automated analysis of atomic resolution images using two-dimensional Gaussian fitting, Adv. Struct. Chem. Imaging 3 (1) (2017) 9.
[31] K.E. MacArthur, H.G. Brown, S.D. Findlay, L.J. Allen, Probing the effect of electron channelling on atomic resolution energy dispersive X-ray quantification, Ultramicroscopy 182 (2017) 264–275.
[32] L. Jones, K.E. Macarthur, V.T. Fauske, A.T.J. Van Helvoort, P.D. Nellist, Rapid estimation of catalyst nanoparticle morphology and atomic-coordination by high-resolution Z-contrast electron microscopy, Nano Lett. 14 (11) (2014) 6336–6341.
[33] A. De Backer, K.H.W. van den Bos, W. Van den Broek, J. Sijbers, S. Van Aert, StatSTEM: an efficient approach for accurate and precise model-based quantification of atomic resolution electron microscopy images, Ultramicroscopy 171 (2016) 104–116.
[34] P. Hartel, H. Rose, C. Dinges, Conditions and reasons for incoherent imaging in STEM, Ultramicroscopy 63 (1996) 93–114.
[35] J.Y. Zhang, J. Hwang, B.J. Isaac, S. Stemmer, Variable-angle high-angle annular dark-field imaging: application to three-dimensional dopant atom profiling, Sci. Rep. 5 (July) (2015) 1–10, https://doi.org/10.1038/srep12419 Available from.
[36] M. Schowalter, A. Rosenauer, J.T. Titantah, D. Lamoen, Temperature-dependent Debye-Waller factors for semiconductors with the wurtzite-type structure, Acta Crystallogr. Sect. A Found. Crystallogr. 65 (3) (2009) 227–231.
[37] B.H. Savitzky, I. El Baggari, C.B. Clement, E. Waite, B.H. Goodge, D.J. Baek, et al., Image registration of low signal-to-noise cryo-STEM data, Ultramicroscopy 191 (2018) 56–65, https://doi.org/10.1016/j.ultramic.2018.04.008 Available from.